Article

Influence of Carbon on Additively Manufactured Ti-6Al-4V

Kerstin Winkler [1,†], Paul Seidel [2,*,†], Andre Danzig [3], Lothar Kroll [1] and Andreas Undisz [2]

1 Institute of Lightweight Structures and Polymer Technology, Chemnitz University of Technology, 09126 Chemnitz, Germany; kerstin.winkler@mb.tu-chemnitz.de (K.W.); slk@mb.tu-chemnitz.de (L.K.)
2 Institute of Materials Science and Engineering, Chemnitz University of Technology, 09125 Chemnitz, Germany; andreas.undisz@mb.tu-chemnitz.de
3 Liebherr-Aerospace Lindenberg GmbH, 88161 Lindenberg, Germany
* Correspondence: paul.seidel@mb.tu-chemnitz.de; Tel.: +49-371531-33290
† These authors contributed equally to this work.

Abstract: In this study, the Ti-6Al-4V powder material for additive manufacturing was mixed with amorphous carbon and processed by powder bed fusion using a laser beam. The specimens were subjected to mechanical and microstructural analyses to investigate the impact of the organic constituent that may become introduced unintentionally as an impurity along the powder handling chain. It is documented that hardness and tensile strength increase with increasing carbon content up to 0.2 wt.%. Above this carbon concentration, extensive crack formation in the samples prevents successful procession.

Keywords: Ti-6Al-4V; carbon; laser melting; powder-bed fusion; organic impurity; strength increase

1. Introduction

The additive manufacturing industry has experienced a boom in many sectors in recent years. One of the most significant areas is the aerospace industry. In 2015, the global market volume of 3D printing processes in aerospace was 430 million euros. By 2030, it is forecasted to reach 9.59 billion euros. This identifies the sector to be one of the fastest-growing industries using additive manufacturing for its needs [1]. The reason for this strong outlook is linked to the challenging limits of conventional manufacturing: lead times are correspondingly long, and the high "buy-to-fly" ratio causes costs to rise [2]. In addition, many aerospace-relevant components are produced in small batch sizes, which means that they have to be developed individually for the aircraft type. Thanks to the many advantages of additive manufacturing, such as tool-free and resource-efficient production, highly complex and functionally integrated components can be generated [3]. Titanium alloys, in particular, which are cost-intensive, are used in aerospace. They combine suitable mechanical properties and very good corrosion resistance with a comparably low material density [4]. In the aerospace industry, laser powder bed fusion of metals (PBF-LB/M) is one of the processes used for additive manufacturing of certain aerospace-related components. In this process, a thin layer of metal powder is applied to a platform by a coating system and fused using a laser beam. The platform is then lowered by a defined layer height, and powder is applied again. The process is repeated until the specified component height is reached [5]. However, before this process can be used as a certified process for the production of aerospace components, aerospace-specific conditions must be fulfilled, and these relate to the entire additive manufacturing chain [6,7]. Titanium alloys, such as Ti-6Al-4V, are gaining importance as materials in the aerospace industry [8]. The Ti-6Al-4V alloy can be processed to exhibit different types of microstructures depending on the temperature and cooling rate: globular, bimodal, and lamellar. The microstructure and material properties of the α + β alloy are tailored by heat treatments [9]. For PBF-L/M, a martensitic microstructure with fine α' lamellae forms due to the high cooling rate of the melting process [10]. Hooper reported that the temperature in the melt is between ~1000

and ~4000 K, and the cooling rates are in the range of 1 to 40 K/μs [11]. To provide the best quality, the metal powder must be free from cross-contamination, and the powder circuit must be closed [12]. Especially re-using titanium alloy powder gains importance in order to reduce waste, but it also raises challenges. Popov et al. documented changes to the microstructure when re-using titanium alloy powder for powder bed fusion. They have shown that titanium alloy powder can be used for powder bed fusion again after hot isostatic pressing was carried out [13]. In another review, the possibilities for re-using such powder were compiled, and the conclusion was drawn that it is important to monitor the powder characteristics, especially possible changes to the chemical composition [14]. Due to the numerous manual steps, such as cleaning out the build chamber or filling, the powder comes into contact with the atmosphere, and the risk of unintentional contamination with other particles or substances increases [15]. In Winkler et al., different sources of organic contamination were intentionally integrated into the PBF-L/M process. The results showed an enormous influence on the properties of the fabricated titanium alloy. Among other things, a new phase was formed [16]. In order to determine how much organic impurities are tolerable in terms of changes to the mechanical properties, carbon was used as an organic contaminant in this study. In contrast to previous work, where the general and qualitative impact of organic contaminants on the successful manufacturing of parts by additive manufacturing was the focus, with the present work, we aim to gain quantitative insight into the impact of specific amounts of organic impurities on the mechanical properties of Ti-6Al-4V.

2. Materials and Methods

2.1. Ti-6Al-4V in PBF-L/M

In this study, the titanium alloy Ti-6Al-4V was used. Additional information, including the chemical composition and physical properties, is published in [16]. The particle size distribution of the used powder was D10 = 23 μm, D50 = 41 μm, and D90 = 61 μm [17]. For microstructure images, the scanning electron microscope (SEM) EM Evo15 from Zeiss was used.

2.2. Preparation of Ti-6Al-4V Powder

To simulate powder contamination with organic material, we blended Ti-6Al-4V powder with carbon. As a carbon source, the so-called 'carbon black' was used, which is an amorphous carbon with a very fine particle size and a very large surface area [18]. We added carbon black to the Ti-6AL-4V powder to set five different concentration levels of carbon according to Table 1. Homogenization of carbon black and titanium powder was carried out by means of sieving equipment from assonic.

Table 1. Concentration levels of carbon black in titanium powder.

Concentration Level	L1	L2	L3	L4	L5
Carbon black in weight-%	0.0	0.01	0.05	0.1	0.2

2.3. Specimen Geometries and Test Scheme

All test specimens were produced with an EOS M290 machine using a layer thickness of 60 μm and argon protection gas. Test cubes, axial fatigue, and static tensile test specimens were fabricated for the subsequent material mechanical tests. The following setup (Figure 1) was realized on the building platform for this purpose.
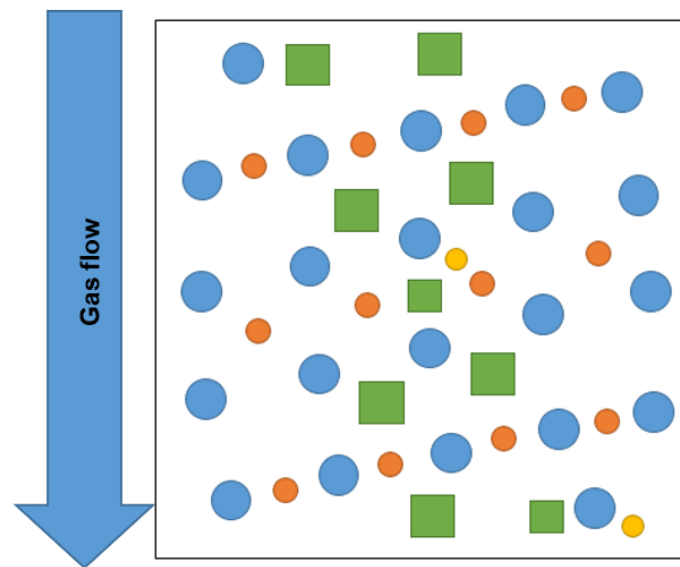
Figure 1. Layout of the build job with test geometries (top view): axial fatigue test specimen (blue), static tensile specimen (orange), test cubes (green), pins (yellow).

All specimens were directly connected to the build platform without additional support structures. For axial fatigue and static tensile testing, cylindrical coupons were built. The dimensions of the as-built specimens are listed in Table 2.

Table 2. Dimensions of the test geometries in as-built state.

Test Specimen	Measurements
axial fatigue	Ø17 mm, height 104 mm
tensile testing	Ø11 mm, height 80 mm
test cubes	edge length 19 mm

The direction of the gas flow is shown in Figure 1. Accordingly, the exposure order of the specimen was chosen against the flow. This was done with regard to the deposition of the weld particles on the powder bed. Because of the dynamic melting process, the welding spatter was distributed on the powder bed by the gas flow. Spatter particles in combination with applied powder potentially led to disturbances in the material, such as pores or missing connection to the underlying layer, when the layer became remelted [19]. After the manufacturing process, the entire build platform with the test specimens was heat-treated in an argon gas furnace; annealing for stress relief was carried out at 675 °C for 4 h. After heat treatment, the final shape of tensile and axial fatigue samples was produced by turning. For the tensile tests, samples of type B6 × 30 with a circular cross-section were used. For the microscopic examinations, the specimen cubes were metallographically prepared.

The geometry of the axial fatigue specimen was manufactured according to DIN 50100. The total length of the specimen was 80 mm, and the test cross-section had a diameter of 6 mm. The specimen was clamped by a hydraulic clamping device. The test was performed under room temperature and stress ratio R = −1 on the hydraulic pulsator test rig 100 from AMR-Hydraulik Chemnitz GmbH. Run out criteria was $1 \cdot 10^7$ cycles. The test plan (Table 3) included seven load levels/stress amplitudes in the range between 450 MPa and 750 MPa. For each load level, at least three tensile specimens were tested. Specimens from different zones of the building area (Figure 2) were mixed for every load level to avoid the systematic impact of the sample position. For the lowest load level, a maximum of two runs was generated.

Table 3. Load levels of the axial fatigue test specimen and zone assignment.

Load Level	Stress in MPa	Sample No.	Zone
1	450	1, 9, 18	M, Z2, Z4
2	500	4, 7, 19	M, Z3, Z4
3	550	13, 16, 22	M, Z1, Z4
4	600	8, 10, 21	M, M, Z1
5	650	2, 6, 15	M, Z2, Z3
6	700	3, 5, 20	M, Z1, Z3
7	750	11, 14, 17	M, Z1, Z4
0	425 resp. 400		
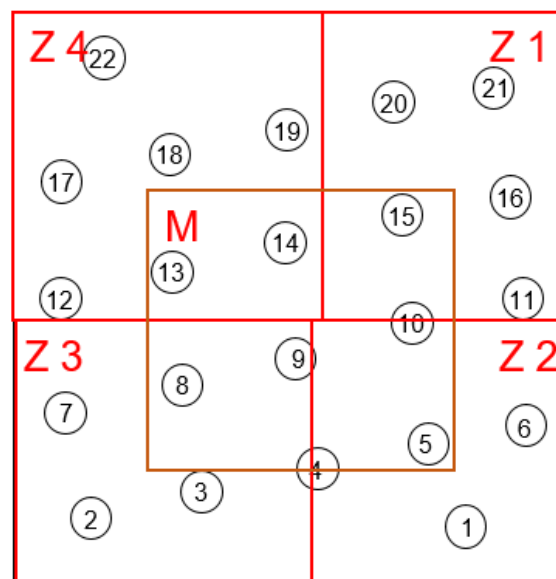
Figure 2. Division of the building area into zones Z1 to Z4 and M for the center.

2.4. Microstrucural Characterization

To investigate the microstructure, it was necessary to prepare the samples. During metallographic preparation, the samples were cut perpendicular to the building direction and hot-mounted in electrically conductive resin in order to prepare cross sections. Afterward, they were ground using silicon carbon paper with grit size 320 and polished using 9 μm diamond suspension for 10 min on a Struers Largo polishing surface. The final polishing was carried out with oxide polishing suspension for titanium on a Struers Chem polishing surface. The oxide polishing was carried out for 10 min. To attain optimal results, the oxide polishing suspension contained 260 mL OP-S, 40 mL hydrogen peroxide, 1 mL nitric acid, and 0.5 mL hydrofluoric acid. After metallographic preparation, all samples were etched for 10 to 20 s using 85 mL distilled water, 10 mL hydrofluoric acid, and 5 mL nitric acid. Initially, an analysis of the test cubes was performed on the GX51 light microscope with the camera SC50 from Olympus. After light microscopic investigation, further investigations were carried out using the SEM LEO1455VP (LEO Electron Microscopy Group, Cambridge, UK).

In order to attain detailed information regarding the microstructure and the chemical composition of the bright and darker regions, transmission electron microscopy (TEM) was carried out using a JEOL ARM 200F NEOARM. For this characterization the bright field detector in scanning TEM Mode (STEM) was used. The measurement was carried out by means of energy-dispersive X-ray spectroscopy (STEM-EDXS).

In this study, the lattice parameters were measured using X-ray diffraction analysis (XRD) utilizing Co K_α-radiation. A parallel beam setup with a 0.5 mm collimator was used for determining the 2θ diffraction angles.

The powder was analyzed using a scanning electron microscope EM Evo15 from Zeiss.

2.5. Mechanical Characterization

To perform the hardness testing, Vickers microhardness testing was carried out using a Buehler's Tukon 1102 device. The testing was performed using HV1 (F = 0.981 N). The Z250 testing machine from Zwick/Roell was used for the static tensile tests. The specimen type B6 × 30 was used. The preload on the test geometries was preset to 10 MPa. The speed for Young's modulus, yield strength, and yield stress were set to 0.5% L_0/min. The test speed was 5% L_0/min.

2.6. Thermogravimetric Analysis

Thermogravimetric analysis was performed using the instrument STA 449F1 by Netsch under a helium atmosphere. The thermogravimetric results have shown that the above-mentioned types of organic contamination decompose by pyrolysis in the temperature range between 350 °C and 540 °C. A small amount of black residue remains, mainly carbon, whereas oxygen, nitrogen, and hydrogen escape as gaseous media. An example of a thermogravimetric analysis is shown in Figure 3.
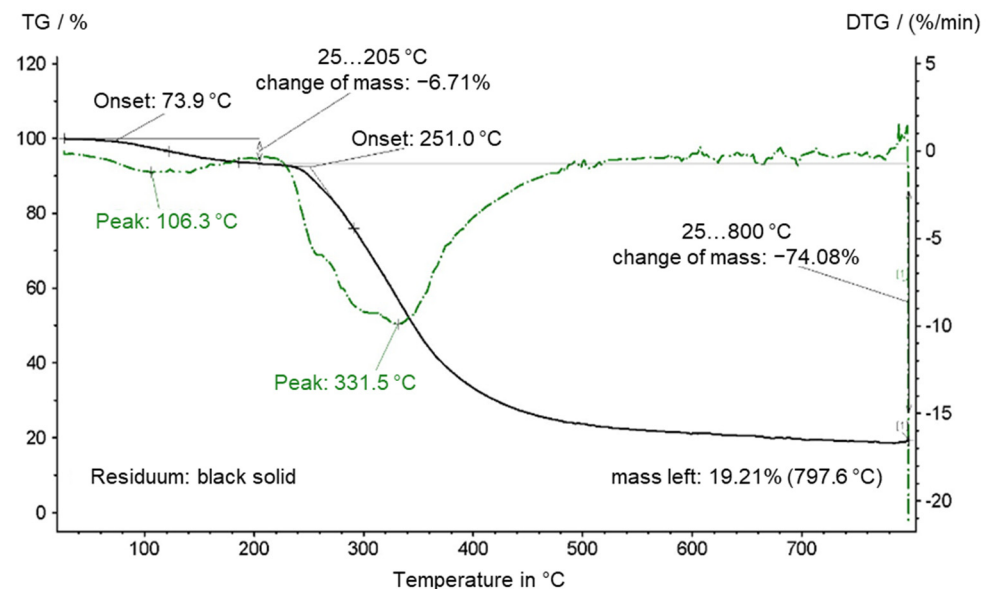

Figure 3. Thermogravimetric analysis of rubber glove snippets.

3. Results

3.1. Powder Analysis

Powder samples were taken for every concentration level and analyzed. Figure 4 shows the powder particles.

As shown in Figure 4, for the concentration of Level L1, a pronounced difference to pure Ti-6Al-4V powder was not observed. For higher carbon concentrations, one or more particles showed locally changed morphology, exhibiting darker regions. The fine carbon particles formed agglomerates at the surface of Ti-6Al-4V particles that appear darker in the SEM images. In L2, a carbon-rich region is marked in green. The higher the concentration of carbon in the powder, the larger the fraction of the surface of individual particles or more particles were affected. In images L5 and L5.2, it is apparent that the carbon agglomerates were not homogeneously distributed on all particles, but the number of completely coated particles increased with carbon concentration. L5.2 shows in lower magnification several Ti-6Al-4V particles with pronounced carbon coating (red arrows) directly situated next to particles with less (yellow marked in L5) or hardly any coating. The particles that did not have significant carbon coatings (yellow highlighted in Figure 4) showed slight carbon agglomerations in the nanometer range only.
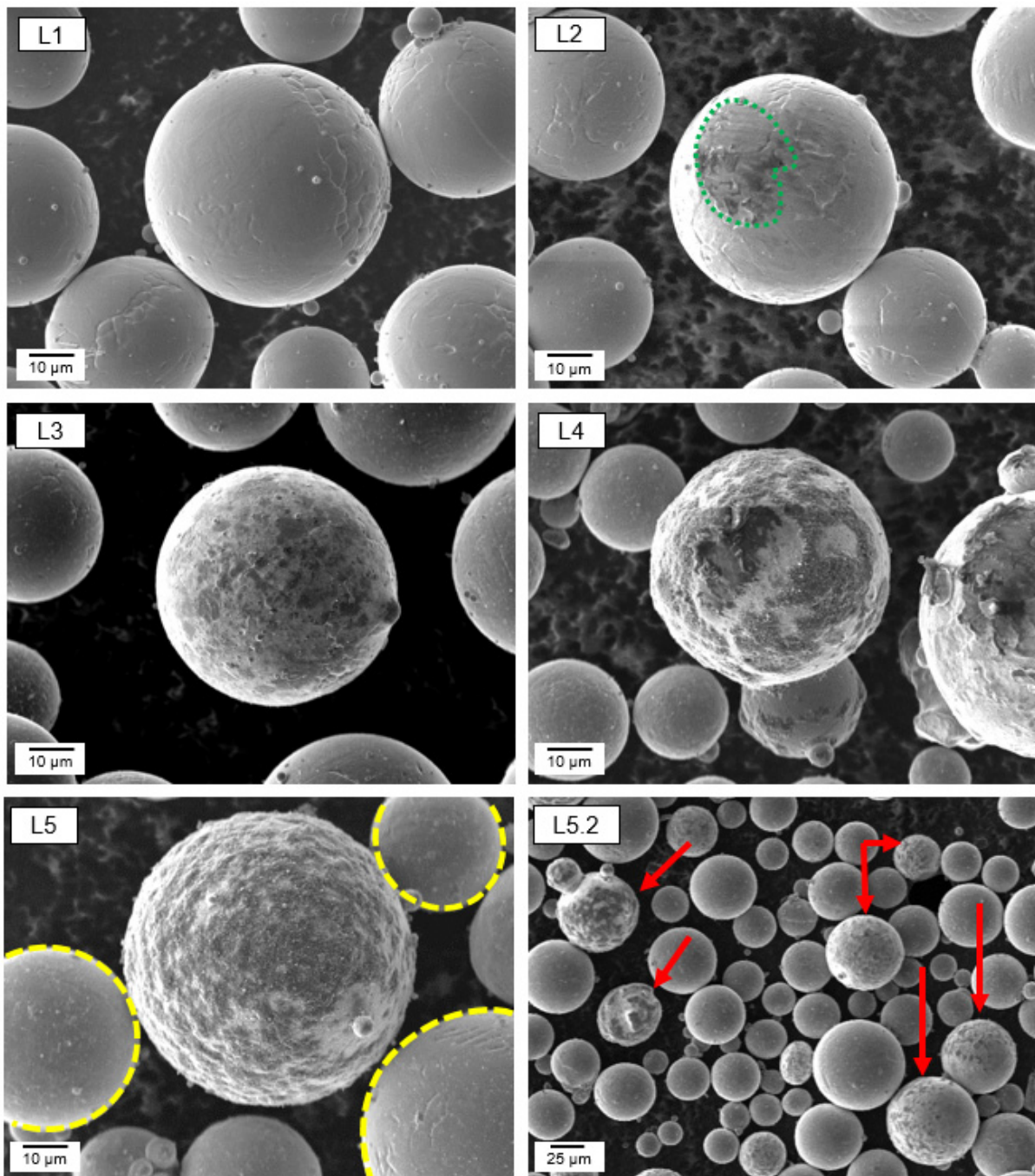
Figure 4. SEM (secondary electron contrast) images of Ti-6Al-4V powder particles with different carbon concentrations levels according to Table 1; yellow particles with slight agglomerations at the surface, red: particles with higher agglomerations.

3.2. Additive Manufacturing

During the processing of the prepared powder, various effects occurred and became visible during or after the manufacturing process. During visual inspection of the test samples with concentration levels L2 to L5, dark inclusions on the surface and occasional cracks, as well as layer offset, were found. Figure 5 shows a selection of these effects.
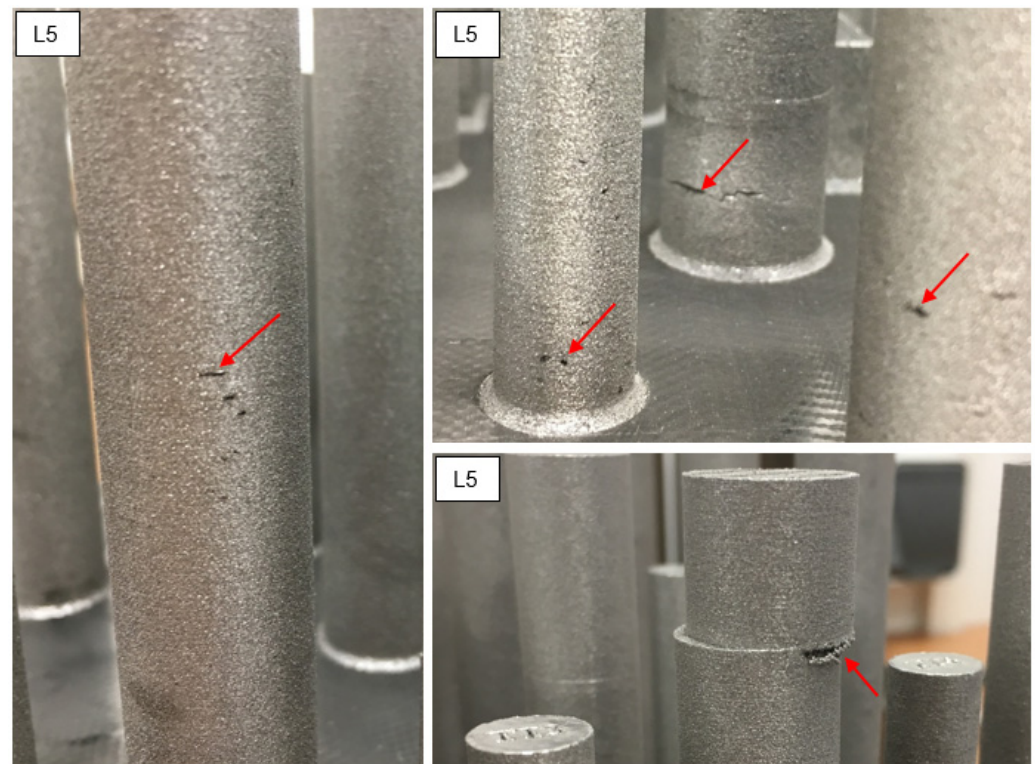
Figure 5. Structures after the building process. Black inclusions, cracks, and layer offset are visible as marked by red arrows. The diameter of the samples is Ø17 mm.

With increasing carbon concentration, more inclusions and cracks in the components became visible. Even for concentration level L2, a few of them occurred. The inclusions can be attributed to the carbon black agglomerations. Furthermore, minor cracks were observed near the connection to the platform and in the distant layers of the tensile specimens. These cracks caused the test samples to tilt a few degrees during the building process. The process did not stop and was exposed partially into the powder bed and partially onto the tilted specimen, creating the layer offset (L5). Exposure to the powder bed resulted in a large melt pool and a rough surface on the downward-facing side of the layer offset, which is shown in Figure 5. For contamination level L5, the building of complete test geometries was no longer possible, and further processing was stopped.

3.3. Microstructure of Ti-6Al-4V Specimen

Figure 6 shows the resulting microstructure for samples with carbon contamination, exhibiting grains and needle-like features, indicating martensite.

The polished and etched sections of the cube specimens show a microstructure with martensitic features and grains that appear to be elongated along the building direction (Figure 6). In several regions of the images, typical imperfections like spherical and irregular pores are visible.

The microstructure in Figure 7 shows darker and lighter regions. Because of the small size of the microstructural features, it was not possible to carry out chemical composition mapping using energy-dispersive X-ray spectroscopy (EDXS). To clarify which phases were formed during SLM, further microstructure investigations with higher local resolution are required.
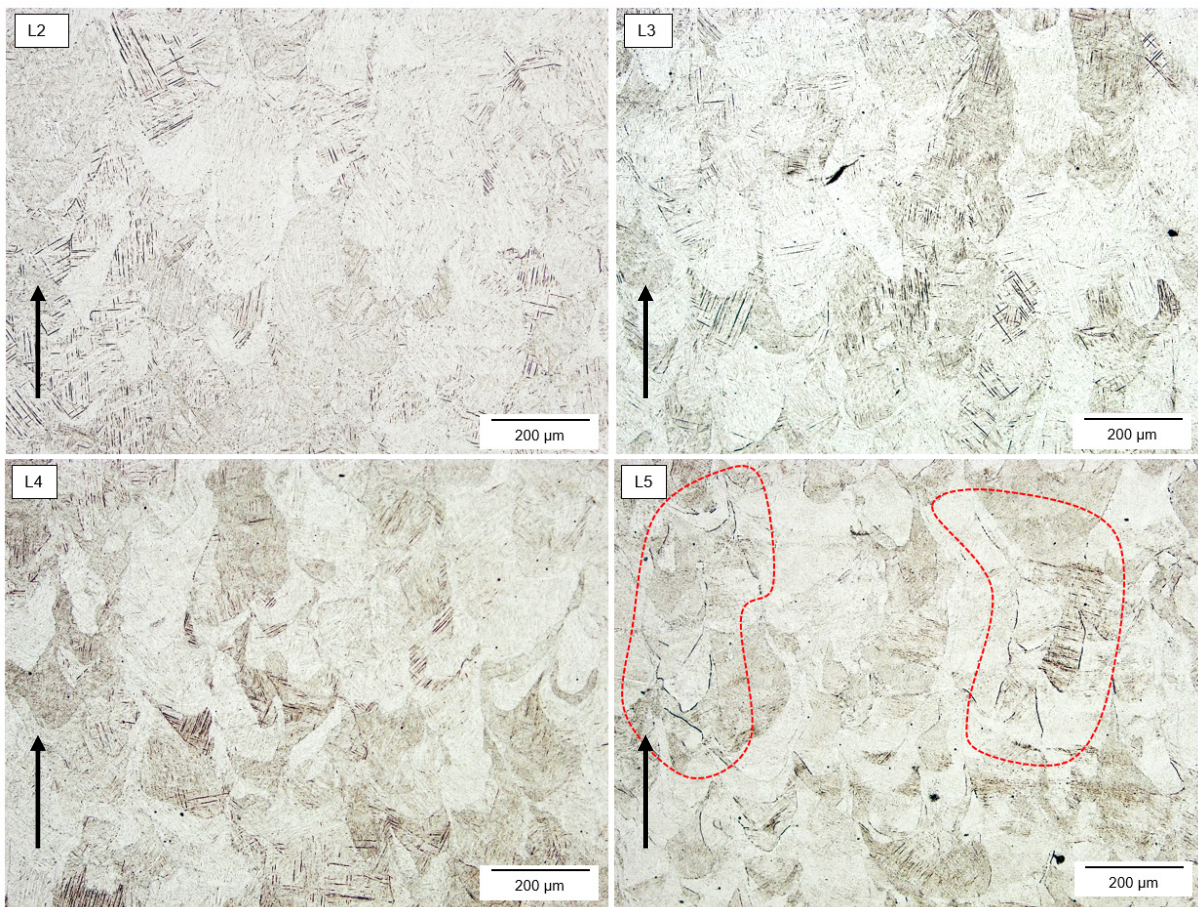
Figure 6. Optical microscope images after metallographic preparation of samples fabricated from Ti-6Al-4V powder containing carbon contamination. The build direction is marked by black arrows.
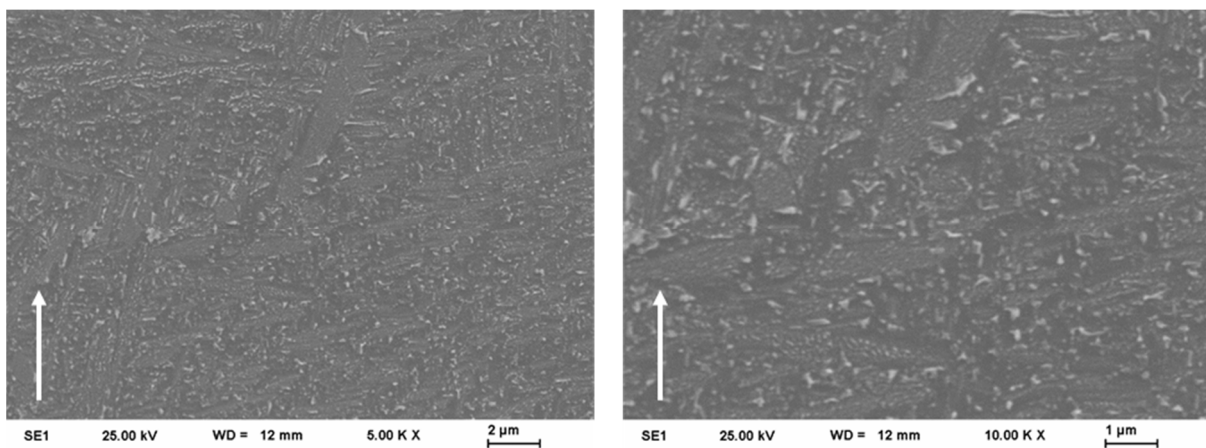

Figure 7. SEM images of processed Ti-6Al-4V samples with 0.2 wt.% carbon concentration, unetched condition using secondary electron contrast. The build direction is marked by white arrows.

3.4. Details of the Microstructure and Elemental Distribution

Figure 8 shows the region of interest on the cross-section sample, where the EDXS analyses was carried out.
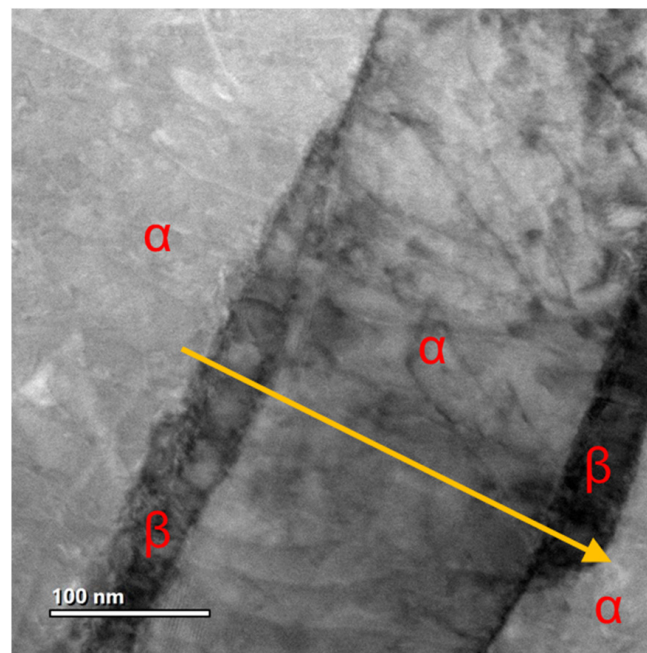
Figure 8. STEM bright-field image of a processed Ti-6Al-4V sample with 0.2 wt.% carbon with an indication of α and β phases; this region of interest was subject to EDXS analyses to access the local chemical composition; the EDXS scan in Figure 11 was attained along the orange line.

Inspired by earlier work on carbon-containing titanium powders, the chemical composition was measured [20]. The local distribution of titanium, vanadium, aluminum, and iron is displayed qualitatively in Figure 9. A qualitative line scan was extracted from the mapping, as shown in Figure 10.
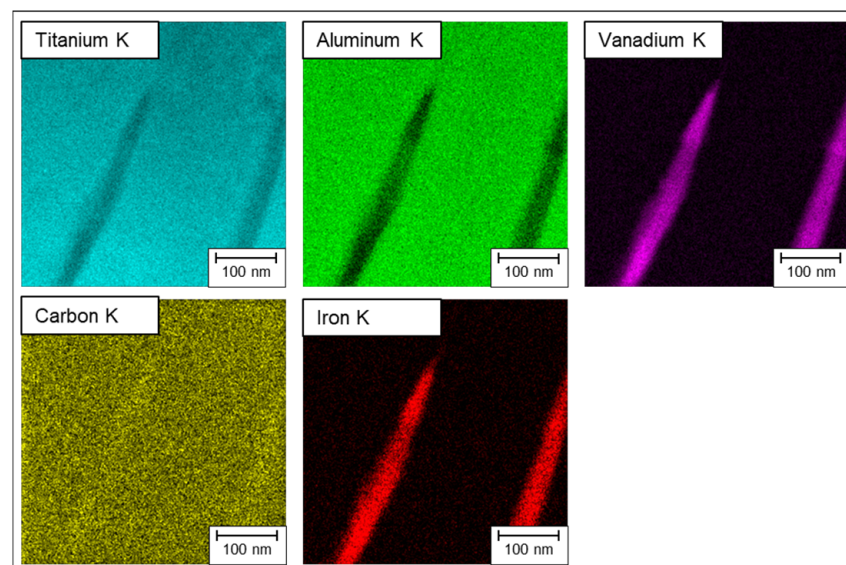
Figure 9. STEM-EDXS-analysis of a processed Ti-6Al-4V sample with 0.2 wt.%, the distribution of carbon is rather homogenous in contrast to the other elements.

According to the measurement, the local microstructure does not contain carbon-rich phases, e.g., TiC. Furthermore, the line scan shows an inhomogeneous distribution of aluminum, iron, and vanadium that indicates the presence of the phases alpha-Ti and beta-Ti, respectively. This is consistent with the result in high-temperature X-ray diffraction analysis [21], where an increased content of vanadium is linked to the β-titanium phase

that is retained even during subsequent heating, especially the line scan substantiates that α- and β-titanium have formed, as they can be distinguished by their different chemical composition, according to Pederson. Interestingly, carbon is distributed homogenously in both phases.
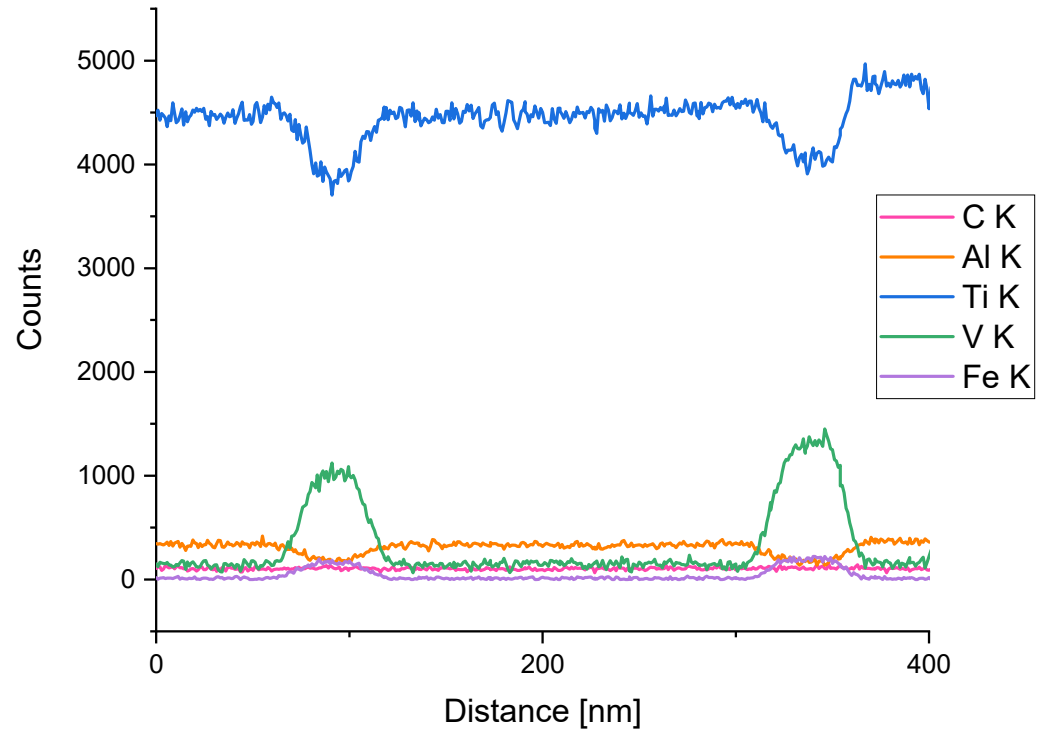

Figure 10. EDXS line scan (qualitative) as measured along the orange line marked in Figure 8.

3.5. Lattice Parameters

The lattice parameters for α-titanium are reported to be a = 2.93 Å and c = 4.67 Å; for β-titanium a = 3.20 Å [22]. The measured lattice parameters for the modified material are shown in Table 4. The volumes of the hexagonal closed packaged structure (α-phase) and the cubic structure (β-phase) were calculated using the following formulas [22]:

Table 4. Lattice parameters of samples with different carbon content were measured by XRD; the volume of the respective unit cells was calculated using Equations (1) and (2).

Concentration Level	α-Ti: a in Å	α-Ti: c in Å	β-Ti: a in Å	α-Ti: V in Å³	α-Ti: c/a Ratio	β-Ti: V in Å³
L1 (0.00%)	2.9921	4.6662	3.1667	34.51	1.5969	31.76
L2 (0.01%)	2.9925	4.6682	3.1770	34.53	1.5973	31.07
L3 (0.05%)	2.9237	4.6696	3.1761	34.57	1.5972	32.04
L4 (0.10%)	2.9222	4.6705	3.1774	34.54	1.5983	32.08
L5 (0.20%)	2.9226	4.6730	3.1800	34.57	1.5989	32.16

Equation (1) (hexagonal structure):

$$V_\alpha = \frac{\sqrt{3}}{2} ca^2 \tag{1}$$

Equation (2) (cubic structure):

$$V_\beta = c^3 \tag{2}$$

For XRD, the powder diffraction files 'PDF#01-089-5009' for α-titanium and 'PDF#00-044-1288' for β-titanium were used. In Figure 11, the calculated volumes are shown in a

diagram and are correlated with the carbon content of each sample. Please note that the calculated unit cell volumes exhibit a clear trend as they increase with the carbon content.
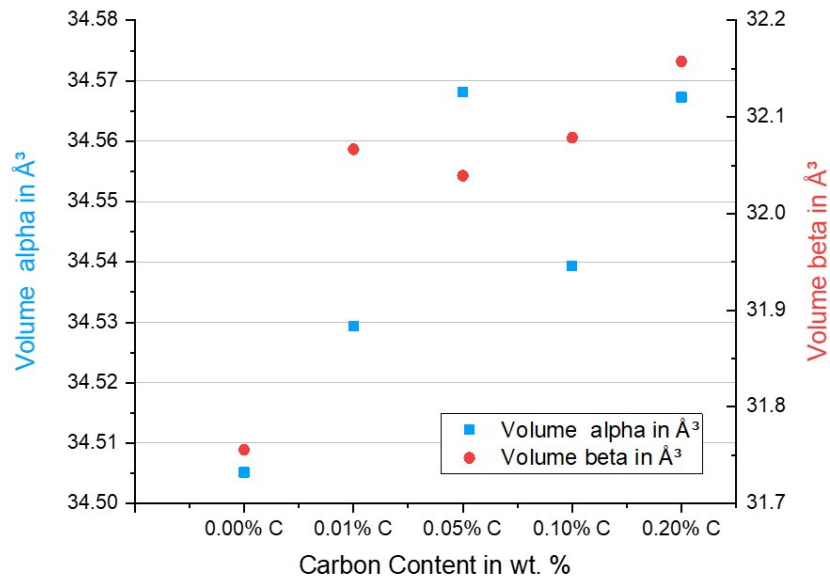

Figure 11. Volume of the respective unit cells of each sample and correlation to the carbon content. The carbon content is shown in weight percent (*x*-axis); the volume of the hexagonal structure (*y*-axis, left) and the cubic structure (*y*-axis, right) is shown in cubic Angstrom.

3.6. Hardness Measurement

To investigate the effect of additional carbon, the hardness of Ti-6Al-4V was measured. The diagram in Figure 12 shows a clear correlation of the average hardness with the carbon concentration: with increasing concentration of carbon, the hardness increases as well.
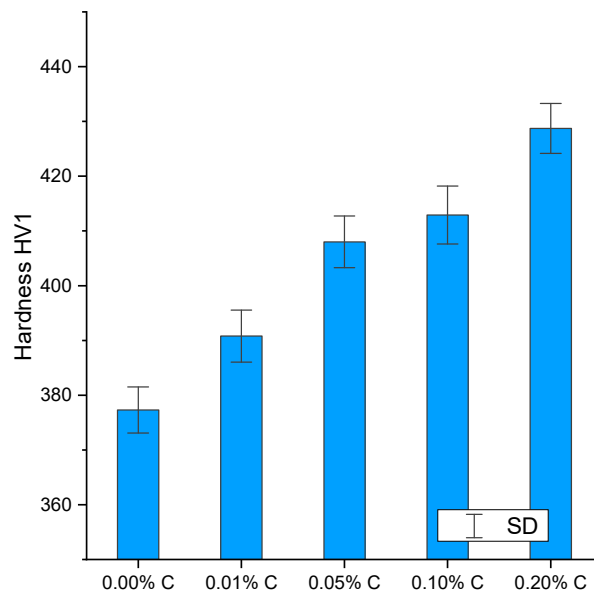

Figure 12. Average hardness of samples with different carbon concentrations levels.

3.7. Tensile Testing

For each contamination level, twelve samples were tested. Table 5 and Figure 13 show the average values of the tensile properties.

Table 5. Tensile properties of the sample with different concentration levels of carbon (average values).

Concentration Level	Yield Strength [MPa]	Tensile Strength [MPa]	Elongation [%]
L1 (0.00%)	1135	1196	13.4
L2 (0.01%)	1150	1217	10.8
L3 (0.05%)	1187	1256	8.6
L4 (0.10%)	1214	1278	8.2
L5 (0.20%)	1290	1339	4.2
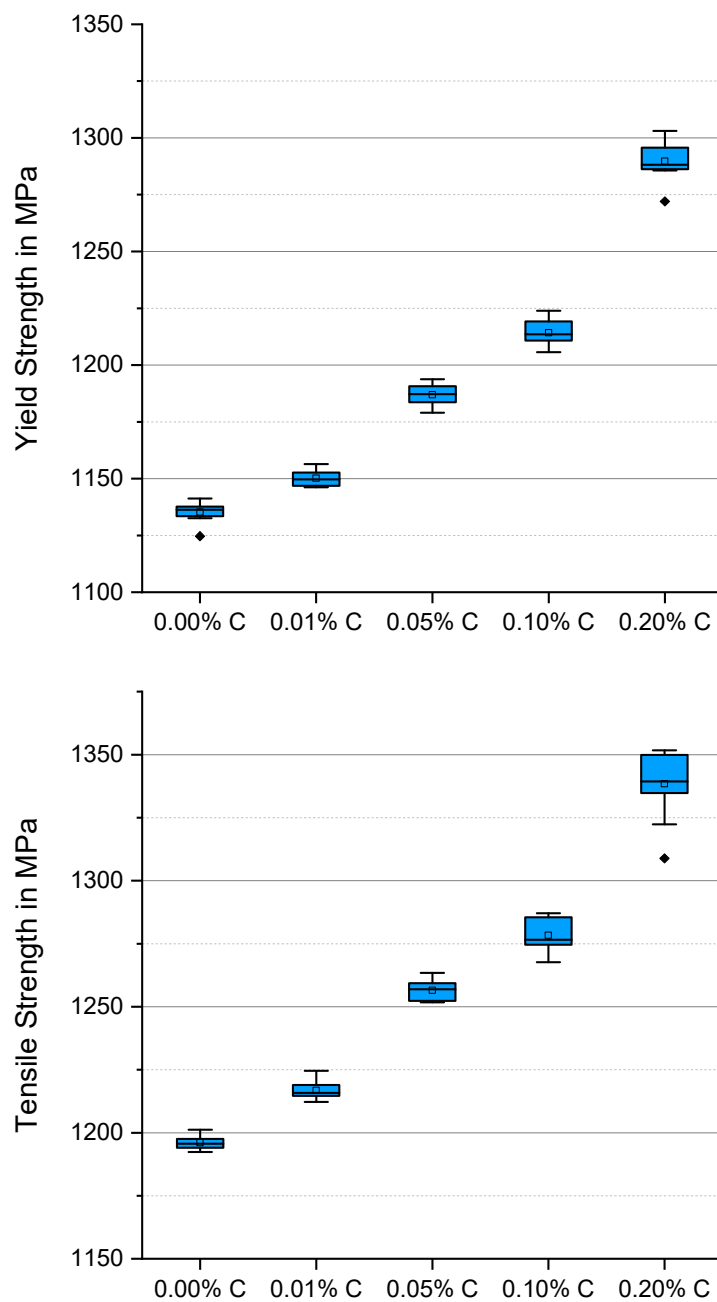
Figure 13. *Cont.*
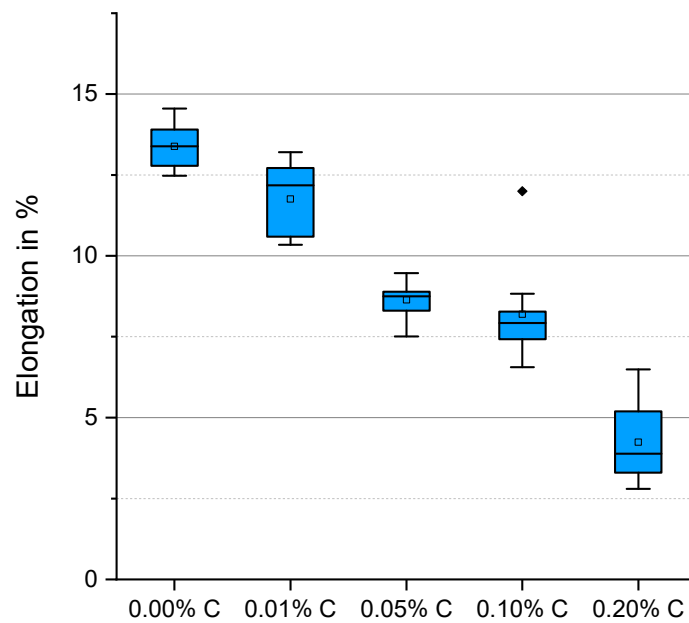
Figure 13. Comparison of the results from the static tensile tests of samples with different carbon content.

With increasing carbon levels, the yield strength and tensile strength increase, whereas the elongation at rupture continuously decreases. Between L1 and L5 of carbon content, the yield strength increases by almost 12% (~154 MPa). The relative increase between the pure Ti-6Al-4V and the highest carbon level is ~11% for tensile strength and ~142 MPa in absolute terms. Simultaneously, the elongation at rupture decreased by ~69% from 13.4% to 4.2%. The boxplot diagrams (Figure 13) clearly highlight the mentioned changes in tensile properties as well as the increasing scattering of data with increasing carbon levels. An unambiguous influence of carbon on static mechanical behavior is obvious.

3.8. Axial Fatigue Testing

Figure 14 shows the results of the axial fatigue testing. Ti-6Al-4V specimens without additional carbon were tested first to provide reference data points (Figure 14). Testing was carried out for the seven load levels. Two run-outs ($>1.0 \cdot 10^7$) were observed for 450 MPa stress amplitude. A third sample with this stress amplitude broke after $1.1 \cdot 10^5$ cycles. A similar scatter over two orders of magnitude was found for load level 650 MPa. The scatter of data, which exceeds the usual level, can be explained by the random occurrence of process inherent defects inside the tested volume.

Because of the extensive cost and time requirements of fatigue testing, focus was set on the carbon concentration levels L2 and L3. Figure 14 shows the results together with the reference material. The data are similar to the reference curve. A trend, if there is one, is masked by the large data scattering.
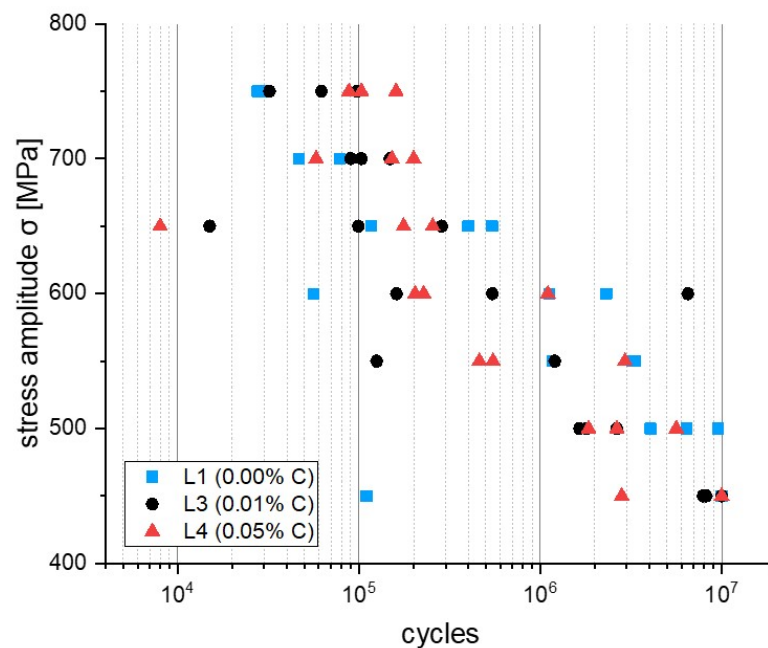
Figure 14. Axial fatigue values for pure Ti-6Al-4V, 0.01%, and 0.05%, carbon.

4. Conclusions

Additive manufacturing of Ti-6Al-4V powder to solid samples was successful up to a carbon concentration of 0.05 wt.%. Accordingly, the processing is rather robust with respect to potential contamination by carbon. At a carbon concentration level of 0.05 wt.%, the successful manufacturing and mechanical properties were severely impaired. This finding is consistent with the solubility limit of carbon in β-titanium of ~0.2 wt.%, which is rather independent of the temperature. Thus, the available carbon is solved in the melt, forming a solid solution with carbon presumably situated at interstitial positions in the lattice. During cooling, carbon remains solved in the lattice even during the transition to α-titanium, which has an even larger solubility level of ~0.4 wt.% at ~920 °C. With decreasing temperatures, the solubility limit of carbon in α-titanium tends towards zero, but the carbon apparently remains in the lattice due to the limited kinetic activation at low temperatures [23]. The microstructure of the specific samples has their respective appearance. Two phases were observed with respect to the distribution of elements, likely α and β. If the carbon concentration exceeds the solubility limit of β-titanium, it is likely that full incorporation into the crystal lattice does not occur, resulting in the formation of cracks that prevent successful manufacturing.

It is interesting to note that the yield and tensile strength show a consistent increase with increasing carbon concentration up to 0.2 wt.%. Simultaneously, the elongation until rupture decreases. Considering that the fatigue behavior does not show a pronounced difference, at least for the samples with lower carbon addition, the increase in strength could provide an advantage for the fabrication of wear resistant structures. The fatigue behavior of Ti-6Al-4V and carbon needs to be investigated in future work. Within this work, two possibilities of strengthening mechanisms are suggested: The addition of carbon is likely to result in solution hardening due to the dissolution into the lattice. This is consistent with the measured increase in the volume of the unit cell. Additionally, it was determined in this work that the addition of carbon results in a mild increase of the c/a ratio in the α-titanium phase towards the ideal c/a ratio of 1.633. In the literature, this is discussed to affect the number of active slip systems for dislocations [24]. When approaching the ideal c/a ratio, the activation of secondary slip systems (pyramidal and primal planes) becomes more difficult, thus increasing yield and tensile strength. The extent of this effect in the present case remains to be assessed in detail in future work.

References

1. Statista. Globales Marktvolumen von 3D-Druck-Verfahren in Ausgewählten Branchen bis 2030 Statista. Available online: https://de.statista.com/statistik/daten/studie/802439/umfrage/globales-marktvolumen-von-3d-druck-verfahren-in-ausgewaehlten-branchen/ (accessed on 26 May 2023).
2. Uckelmann, I. *'Buy-to-Fly' Ratio Cutting Costs with Metal 3D Printing*; Materialise Manufacturing: Leuven, Belgium, 2017.
3. Liu, R.; Wang, Z.; Sparks, T.; Liou, F.; Newkirk, J. 13—Aerospace applications of laser additive manufacturing. In *Laser Additive Manufacturing: Materials, Design, Technologies, and Applications*; Brandt, M., Ed.; Elsevier/Woodhead Publishing: Amsterdam, The Netherlands, 2016; pp. 351–371. ISBN 978-0-08-100433-3.
4. Dutta, B.; Froes, F.H. (Eds.) Chapter 1—The Additive Manufacturing of Titanium Alloys. In *Additive Manufacturing of Titanium Alloys*; Butterworth-Heinemann: Oxford, UK, 2016; pp. 1–10, ISBN 978-0-12-804782-8.
5. Yadroitsev, I. *Fundamentals of Laser Powder Bed Fusion of Metals*; Elsevier: Amsterdam, The Netherlands, 2021; ISBN 9780128240915.
6. Russell, R.; Wells, D.; Waller, J.; Poorganji, B.; Ott, E.; Nakagawa, T.; Sandoval, H.; Shamsaei, N.; Seifi, M. 3—Qualification and certification of metal additive manufactured hardware for aerospace applications**Disclaimer: The views presented in this paper are those of the authors and should not be construed as representing official rules interpretation or policy of ASTM International, General Electric (GE), Lockheed Martin Corporation (LMCO), National Aeronautics and Space Agency (NASA), Japanese Space and Exploration Agency (JAXA), or the Federal Aviation Administration (FAA). In *Additive Manufacturing for the Aerospace Industry*; Froes, F., Boyer, R., Eds.; Elsevier: Amsterdam, The Netherlands, 2019; pp. 33–66. ISBN 978-0-12-814062-8.
7. Blakey-Milner, B.; Gradl, P.; Snedden, G.; Brooks, M.; Pitot, J.; Lopez, E.; Leary, M.; Berto, F.; du Plessis, A. Metal additive manufacturing in aerospace: A review. *Mater. Des.* **2021**, *209*, 110008. [CrossRef]
8. Katz-Demyanetz, A.; Popov, V.V.; Kovalevsky, A.; Safranchik, D.; Koptyug, A. Powder-bed additive manufacturing for aerospace application: Techniques, metallic and metal/ceramic composite materials and trends. *Manuf. Rev.* **2019**, *6*, 5. [CrossRef]
9. Handke, V. *Kornfeinung von Titanschweißnähten Durch Mechanisch-Thermische Behandlung. Diplomarbeit*; Hochschule für Angewandte Wissenschaften Hamburg: Hamburg, Germany, 2012.
10. Wycisk, E. *Ermüdungseigenschaften der Laseradditiv Gefertigten Titanlegierung TiAl6V4*; Springer: Berlin/Heidelberg, Germany, 2017; ISBN 978-3-662-56059-4.
11. Hooper, P.A. Melt pool temperature and cooling rates in laser powder bed fusion. *Addit. Manuf.* **2018**, *22*, 548–559. [CrossRef]
12. *DIN SPEC 17071:2019-12*; Additive Fertigung_- Anforderungen an Qualitätsgesicherte Prozesse für Additive Fertigungszentren. Beuth Verlag GmbH: Berlin, Germany, 2019; (In German and English)
13. Popov, V.V.; Lobanov, M.L.; Stepanov, S.I.; Qi, Y.; Muller-Kamskii, G.; Popova, E.N.; Katz-Demyanetz, A.; Popov, A.A. Texturing and Phase Evolution in Ti-6Al-4V: Effect of Electron Beam Melting Process, Powder Re-Using, and HIP Treatment. *Materials* **2021**, *14*, 4473. [CrossRef] [PubMed]
14. Powell, D.; Rennie, A.E.; Geekie, L.; Burns, N. Understanding powder degradation in metal additive manufacturing to allow the upcycling of recycled powders. *J. Clean. Prod.* **2020**, *268*, 122077. [CrossRef]
15. Seyda, V. *Werkstoff- und Prozessverhalten von Metallpulvern in der Laseradditiven Fertigung*; Springer: Berlin/Heidelberg, Germany, 2018; ISBN 978-3-662-58232-9.
16. Winkler, K.; Ahmad, H.; Danzig, A.; Gloetter, P.; Schubert, F.; Wagner, G.; Kroll, L. Effect of organic impurity in additive manufactured Ti-6Al-4V. *Addit. Manuf. Lett.* **2023**, *5*, 100116. [CrossRef]
17. AP&C. *Material Certificate No: MC-17-0120: Ti-6Al-4V Grade 23 Powder*; AP&C: Quebec, QC, Canada, 2017.

18. Jäger, C.; Henning, T.; Schlögl, R.; Spillecke, O. Spectral properties of carbon black. *J. Non-Cryst. Solids* **1999**, *258*, 161–179. [CrossRef]

19. Wang, D.; Wu, S.; Fu, F.; Mai, S.; Yang, Y.; Liu, Y.; Song, C. Mechanisms and characteristics of spatter generation in SLM processing and its effect on the properties. *Mater. Des.* **2017**, *117*, 121–130. [CrossRef]

20. Mereddy, S.; Bermingham, M.J.; Kent, D.; Dehghan-Manshadi, A.; StJohn, D.H.; Dargusch, M.S. Trace Carbon Addition to Refine Microstructure and Enhance Properties of Additive-Manufactured Ti-6Al-4V. *JOM* **2018**, *70*, 1670–1676. [CrossRef]

21. Pederson, R. Microstructure and Phase Transformation of Ti-6 Al-4 V ROBERT PEDERSON. Doctoral Dissertation, Luleå Tekniska Universitet, Luleå, Sweden, 2002.

22. Swarnakar, A.K.; van der Biest, O.; Baufeld, B. Thermal expansion and lattice parameters of shaped metal deposited Ti–6Al–4V. *J. Alloys Compd.* **2011**, *509*, 2723–2728. [CrossRef]

23. Steiner, R. *Metals Handbook, 5. Print*; ASM International: Metals Park, OH, USA, 1997; ISBN 0-87170-377-7.

24. Peters, M. *Titan und Titanlegierungen*, 3rd ed.; Wiley-VCH: Weinheim, Germany, 2002; ISBN 3527305394.